Journal of Power Sources Advances 26 (2024) 100141

Contents lists available at ScienceDirect

Journal of Power Sources Advances

journal homepage: www.sciencedirect.com/journal/journal-of-power-sources-advances

Influence of the mixing speed in the rheology of NMC622-based Li-ion battery electrode slurries

Diana Zapata Dominguez [a,b], Jiahui Xu [a,b], Yasmina Boudjema [a], Siwar Ben Hadj Ali [a], Franco M. Zanotto [a,b], Alejandro A. Franco [a,b,c,d,*]

[a] Laboratoire de Réactivité et Chimie des Solides (LRCS), UMR CNRS 7314, Université de Picardie Jules Verne, Hub de l'Energie, 15, rue Baudelocque, 80039, Amiens, Cedex, France
[b] Réseau sur le Stockage Electrochimique de l'Energie (RS2E), FR CNRS 3459, Hub de l'Energie, 15, rue Baudelocque, 80039, Amiens, Cedex, France
[c] Alistore European Research Institute, FR CNRS 3104, Hub de l'Energie, 80039, Amiens, France
[d] Institut Universitaire de France, 103 boulevard Saint Michel, 75005, Paris, France

ARTICLE INFO

Keywords:
Mixing speed
NMC622
Positive electrode
Rheology measurements
Coarse-Grained Particle Dynamics modeling
Combinatory approach

ABSTRACT

Finding a correlation between the rheology of an electrode slurry and the mixing variables is challenging due to the complex interactions among the materials in the suspension. Here, we report a systematic study of the mixing speed and how this variable impacts the slurry rheology of the Nickel Manganese Cobalt Oxide (NMC622) positive electrode at 2000, 3000, and 4000 rpm and maintaining constant the other mixing parameters. We partially combined the slurry components and compared the rheology results with the complete formulation. This systematic study shows differences in viscosity depending on mixing speed and the slurry component combination. In addition, frequency oscillatory sweeps were used to obtain information on the slurry microstructure, showing changes depending on the nature of component interactions. The slurries were also casted, dried, and calendered. Numerical simulations were also performed to analyze the experimental findings. Understanding the slurry rheology and the interaction of the formulation components is fundamental for further engineering electrode manufacturing and analysis of the dried electrode's output properties.

1. Introduction

Lithium-ion batteries (LIBs) as a marketable product are gradually increasing in production due to the promotion of battery electric vehicles (BEVs). Since 2020, multiple battery gigafactories are springing up in Europe. At the same time, some challenges must be addressed, such as insufficient battery energy density and the cost of battery raw materials that prevent the decrease of BEV's cost and constrain their wide utilization. In that context, assisting battery manufacturing production by computationally simulating the fabrication process of electrodes, supported by targeted experiments, could significantly reduce time, labor, and material costs [1,2].

Slurry mixing, the primary step in the LIB manufacturing process, plays a significant role in electrode quality. First, choosing the proper materials and balancing the proportions between different components is crucial to maximizing their efficiency by exploring various formulations. Currently, the most commonly used active materials (AMs) for BEVs' positive electrodes are Nickel Manganese Cobalt Oxide (NMC) and Lithium Iron Phosphate (LFP). The positive electrodes typically consist of AM, conductive carbon, and polymer binders. In the industry, the processing route for the positive electrode slurry that is predominantly used involves using polyvinylidene fluoride (PVDF) as the binder, N-methyl pyrrolidone (NMP) as the solvent, and carbon black (CB) to increase the conductivity of the electrode [3]. Second, the mixing conditions are also influential factors in dispersing the materials, minimizing the size of aggregates, and providing the optimal arrangement of AM, CB, and binder. Creating an appropriate conductive network throughout the electrode depends on the interaction among the different components, which play a crucial role in the output physical and electrochemical properties of the electrode [4].

Several studies have been carried out on the significant changes in the slurry or electrode's mechanical, structural, and electrical properties by changing the mixing process parameters or protocol. For NMC-based slurry production, the mixing protocol has been investigated by

* Corresponding author. Laboratoire de Réactivité et Chimie des Solides (LRCS), UMR CNRS 7314, Université de Picardie Jules Verne, Hub de l'Energie, 15, rue Baudelocque, 80039 Amiens, Cedex, France.
E-mail address: alejandro.franco@u-picardie.fr (A.A. Franco).

https://doi.org/10.1016/j.powera.2024.100141
Received 20 December 2023; Received in revised form 30 January 2024; Accepted 4 February 2024
Available online 13 February 2024

changing the order in which the components are mixed. For instance, mixing CB with PVDF before adding NMC has been reported to give a more stable slurry than combining the premix NMC + CB and PVDF + NMP [5]. The former sequence has been reported to create clusters of CB/PVDF around the NMC and provide high C-rate capability. The influence of the temperature ranges between 25 °C and 75 °C during the mixing has been studied for NMC532. The main results show that the viscosity decreases by 23 % when coated at 60 °C *vs*. 25 °C. Therefore, increasing the temperature when mixing could accelerate positive electrode manufacturing by increasing the coating speed [6].

Several studies based on physical computational modeling have been done to study the mechanical behavior during the mixing process. Mayer *et al.* used the Discrete Element Method (DEM) to simulate the behavior of nanoscale carbon black aggregates represented by spherical particle clusters during the dispersion process [7]. Asylbekov *et al.* conducted simulations on the dispersion process of cathode slurries in a planetary mixer, studying the breaking of conductive carbon aggregates during the process [8]. Similarly, they also developed a dry mixing model based on the population balance equation and DEM to investigate the particle size changes of carbon black during the dry mixing and gain a better understanding of the mechanisms involved in the comminution process [9]. However, all these previously reported models are unable to investigate AM particle dispersion.

One of the critical parameters that could impact the conductive additive network upon the slurry drying is selecting an appropriate stirring speed. The interaction between the formulation components and manufacturing parameters makes identifying the actual speed effect challenging. Here, we sequentially change the mixing speed at 2000, 3000, and 4000 rpm by keeping constant premixing and mixing parameters (i.e., temperature, mixing time) to capture the influence in the rheology of the slurry. In addition, a combinatory methodology for the formulation and a model is also designed to understand the interaction between materials and their effect on the slurry. Finally, the slurries produced under different conditions were casted, dried, and calendered. Tomography data was used in order to create stochastic structures with the correct sizes, allowing for comparison of the microstructures in terms of tortuosity factors.

2. Materials and methods

2.1. Experiment

The electrode slurry was prepared with 94 wt% $LiNi_{0.6}Mn_{0.2}Co_{0.2}O_2$ (NMC 622, Targray, denoted as NMC), 3 wt% carbon black (C-NERGYTM super C45, represented as CB), 3 wt% PVDF (Solvay, denoted as PVDF). The powder components were first premixed overnight in a Turbula® mixer. Then, the NMP solvent was added until the desired solid content of 60 % was achieved. A Dispermat CV3-PLUS high-shear mixer was used for the NMP-based slurry preparation for 2 h at 25 °C with three different mixing speeds: 2000, 3000, and 4000 rpm. Mixed slurries consisting of NMC + CB + PVDF, NMC + CB, and CB + PVDF were also prepared for rheological measurements, as shown in Table 1.

The rheological measurements were acquired by applying a shear rate ramp (0.1–700 Hz) immediately after the slurry preparation using a rheometer (Kinexus lab+, Netzsh) at a constant height of 1 mm between the bottom and top plates. In the frequency sweep, the tests were carried out between 0.1 and 20 Hz, while the deformation amplitude was kept constant at 0.26 Pa for NMC + CB + PVDF and CB + PVDF. In comparison, the deformation amplitude for NMC + CB was kept at 0.3, 0.07, and 0.02 Pa for 2000, 3000, and 4000 rpm, respectively. These deformation amplitude values correspond to the obtained linear viscoelastic region. All rheological measurements were performed at 25 °C.

The resulting electrode slurries were then coated over a 23 μm thick aluminum current collector using a comma-coater prototype-grade machine, fixing the coating speed at 0.3 m/min with a constant comma gap of 200 μm. The electrode was dried in a built-in two-part oven at 80 °C and 95 °C.

Porosities were calculated according to the following Equation (1):

$$\varepsilon = 1 - \frac{m_{el}\left(X_{NMC}/\rho_{NMC} + X_{CB}/\rho_{CB} + X_{PVDF}/\rho_{PVDF}\right)}{V_{el}} \quad (1)$$

where X and ρ are the mass fractions in the electrode and densities of the three solid components and m_{el} and V_{el} correspond to the electrode mass and volume, respectively. The electrode mass loading and thickness were measured in different areas on the electrode film. The porosity for the calendered electrodes was calculated using Equation (1) for ten different electrode cuts from the electrode sheet. The properties of the electrodes are presented in Table 2.

The electrodes were calendered with a prototype-grade lap press calender (BPN250, People & Technology, Korea). The latter consists of a two-roll compactor of 25 cm in diameter. The gap between the rolls was set to reach 30 % of compression. The calendering was performed at constant line speed (0.54 m/min) and 60 °C. The porosity for the calendered electrodes was calculated using Equation (1) for ten different electrodes cut from the electrode, with results summarized in Table 2.

Electrochemical Impedance Electrochemistry (EIS) tests in symmetric cells were performed in 2035-type coin cells assembled in a dry room (H_2O concentration < 15 ppm). The coin cells (both on the positive and negative side) were assembled using Celgard 2500 as separator (thickness = 25 μm, porosity = 55%). The deposited electrodes had a diameter of 13 mm. The electrolyte was a 10 mM $TBAClO_4$ solution prepared in a 1:1 wt% mixture of ethylene carbonate: dimethyl carbonate (volume = 100 μL). The EIS tests were performed with an MTZ-35 impedance analyzer (BioLogic, Seyssinet-Pariset, France) in 10^{-1} – 10^{7} Hz with a potential perturbation of 5 mV for five different symmetric cells per calendering condition. All measurements were carried out at 25 ± 1 °C. All measurements were carried out at 25 ± 1 °C. The electrolyte conductivity and geometric area were 3.12 ×10^{-4} S/cm at 25 °C. and 1.33 ×10^{-3} cm^2, respectively. From the determined ionic resistance values

Table 2
Main characteristics of the dried electrodes when using a comma gap of 200 μm.

Mixing speed [rpm]	Electrode	Mass loading [mg/cm^2]	Thickness [μm]	Porosity [%]	Tortuosity [%]
2000	Pristine	18.4 ± 0.4	111 ± 1	47 ± 1	2.1 ± 0.2
	Calendered 30%		85 ± 1	24 ± 1	2.2 ± 0.2
3000	Pristine	18.6 ± 0.4	113 ± 1	48 ± 1	1.9 ± 0.1
	Calendered 30%		82 ± 1	24 ± 1	2.0 ± 0.3
4000	Pristine	18.7 ± 0.4	113 ± 1	48 ± 2	1.9 ± 0.3
	Calendered 30%		82 ± 1	26 ± 2	3.0 ± 0.2

Table 1
Mixed formulations for rheological measurements.

	94 wt% NMC +3 wt% CB + 3 wt% PVDF			97 wt% NMC +3 wt% CB		50 wt% CB + 50 wt% PVDF	
Solid content [%]	60.00 ± 0.08			60.00 ± 0.02		5.7 ± 0.02	
Slurry components	**NMC**	**CB**	**PVDF**	**NMC**	**CB**	**CB**	**PVDF**
Mass (g)	26.000 ± 0.005	0.830 ± 0.001	0.830 ± 0.001	25.00 ± 0.05	0.774 ± 0.001	0.716 ± 0.003	0.7118 ± 0.0005

R_{ion}, the ionic conductivity σ, the geometric area A, the electrode porosity ε, and thickness d, we calculate the trough-plane tortuosity factor from the following Equation (2). R_{ion} and tortuosity were found for the five different symmetric cells per condition.

$$\tau = \frac{R_{ion}\sigma A\varepsilon}{2d} \tag{2}$$

2.2. Simulation

A mesoscale physical computational model based on Coarse-Grained Particle Dynamics (CGPD) has been developed to investigate the impact of the rotation speed of the mixer on particle-pairs distance distribution during the solvent dispersion process. Conceptually, this model shares the mesoscopic viewpoint of our previously reported models of electrode slurries [10,11]. The scale of our slurry mixing model is confined within a container with a diameter of 100 μm and a height of 150 μm to strike a balance between computational cost and the representativeness of the model. We are aware that our model system is much smaller than a real mixer. Still, it allows us to qualitatively investigate the inter-particle behavior to support the understanding of our experiments. The geometric construction of the container and mixer used in our model is illustrated in Fig. S1 in the Supporting Information. In the simulation, the AMs and the pseudo-carbon-binder-domain (CBD) are represented by spherical particles, and they are used both explicitly and implicitly to describe the carbon black, polymer binder, and solvent, as detailed in the Supporting Information and illustrated in Fig. S2. AM particles present a particle size distribution (PSD) similar to the experimental electrode slurry, which was extracted by X-ray Computed Tomography (XCT). AM and CBD masses in the model are in accordance to their experimental 94% AM - 6% CBD mass ratio. Details on the simulation process are also shown in the Supporting Information, and an example of mixing simulation is illustrated in a supplementary video. The simulations are performed by using the open-source molecular dynamics simulator software LAMMPS [12]. A timestep of 0.5 ns was used after verifying numerical stability. The computation simulation duration is within two days. These were run in 32 cores Intel(R) Xeon(R) CPU E5-2680 v4 @ 2.40 GHz in 1 node (128 GB of RAM) of the MatriCs platform (Université de Picardie-Jules Verne, France).

For the computer-generated electrodes, the morphology of dried and calendered electrodes was stochastically recreated through our INNOV algorithm [13]. The different properties of the computer-generated electrodes, such as porosity and tortuosity factor, were compared with the experimental results. The ionic tortuosity factor of these computer-generated electrode microstructures was calculated through the DiffuDict module of GeoDict 2023 (Math2Market). For the diffusivity calculation, Fick's first law is solved throughout the whole domain. The diffusion coefficient within the pores was set at 1 m^2s^{-1}, while the diffusion within the CBD domain was calculated according to the Bruggeman relationships ($D_{eff,CBD} = D_{bulk} \times \varepsilon^{1.5}$), where ε stands for the CBD nanoporosity, 50 % for non-calendered electrode microstructures and 27% for calendered electode microstructures, and D_{bulk} and $D_{eff,CBD}$ stand for the electrolyte diffusivity in the pore and in the CBD phases, respectively. The resulting value was $D_{eff} = 0.14\, m^2s^{-1}$. The electrode tortuosity factor (τ) was calculated according to the McMullin number [14] ($N_M = \frac{D_{bulk}}{D_{eff,electrode}} = \frac{\tau}{\varepsilon}$), where ε is the electrode porosity. All of these input parameters were considered isotropic. Dirichlet boundary conditions were assumed for all external planes.

3. Slurry results and discussion

The manufacturing of electrodes involves interconnected processes and variables, influencing the output properties at each stage of electrode fabrication. In this study, we systematically change the mixing speed in the slurry to assess the effect of the output properties on the rheology of NMC-based slurry and develop the physical computational models to understand the experimental results.

3.1. Effect of the mixing speed in the slurry viscosity

A higher mixing speed is expected to separate the material agglomeration, increasing the coating processability efficiently [15]. However, the effect of the mixing speed for positive and negative electrodes may highly depend on the binder's mechanical properties. We compared the mixing speed effect in slurries containing NMC622 at 2000, 3000, and 4000 rpm. The slurry protocol was kept constant among the samples (see Experimental Section). In addition, we sequentially combine each formulation component to disentangle their effect in the slurry rheology [16,17], as shown in Table 1.

The mixing speed affects the rheology depending on the binder properties and stability, resulting in a material rearrangement caused by the energy input. Fig. 1 shows the effect of mixing speed on the viscosity along the shear rate by comparing mixtures of a) NMC + CB + PVDF, b) NMC + CB, and c) CB + PVDF.

For both NMC-containing slurries, the viscosity increases at a lower mixing speed (see Fig. 1a and b). In contrast, the mixture's viscosity containing CB + PVDF remains constant for the different mixing speeds with viscosity tendency and values close to NMC + CB + PVDF.

Various studies have proposed that CB and PVDF tend to adsorb to active materials like NMC and graphite, which could impact the output properties of slurries and coated electrodes, such as electrode adhesion, tortuosity factor, and electrochemical performance [16–19]. The lower viscosity obtained for the slurry NMC + CB + PVDF mixed at 4000 rpm compared with 2000 and 3000 rpm (see Fig. 1a) could be explained by a possible decrease of CB agglomerates (destroyed due to the high mixing speed) and higher adsorption of PVDF and CB to the NMC particles [17]. CB and NMC + CB networks may be quite sensitive to being broken by the mixing process, reflected in the remarkable viscosity change when comparing the mixing speeds at 2000, 3000, and 4000 rpm (see Fig. 1b) [16]. The dispersion speed of 4000 rpm used in NMC + CB may cause a decrease in free CB because it will preferentially be adsorbed to NMC, considerably decreasing the slurry viscosity (see Fig. 1b).

3.2. Influence of mixing speed on the frequency sweeps of the slurry

Frequency sweeps are performed by maintaining the strain constant to evaluate further the effect of mixing speed in the slurry response. Fig. 2 shows the viscous (G″) and elastic (G′) moduli for the three different mixing speed conditions in the mixtures of a) NMC + CB + PVDF, b) NMC + CB, and c) CB + PVDF, respectively. For PVDF-containing slurries, the tendency is mostly elastic (G' > G″) (see Fig. 2a and c). Particularly, for NMC + CB + PVDF, the G′ and G″ will evolve depending on the frequency and mixing speed. For instance, at 2000 rpm, G′ and G″ are approaching without converging. Whereas at 3000 rpm, G′ equals G″ at ~8 Hz and overlaps up to 20 Hz. Regarding the 4000 rpm, G′ and G″ get closer and cross over at ~2.5 Hz, changing to a viscous-like tendency (G" > G′). In contrast, the NMC + CB presents a viscous-like or solid-like trend (G" > G′) until ~ 2 Hz. However, G' and G" curves show instabilities when increasing the frequency rate (see Fig. 2b), meaning that these dispersions are not stable [16].

The NMC + CB has a viscous behavior that evolves to elastic-like when PVDF is included in the complete slurry composition (see Fig. 2a). The PVDF stabilizes and gives an elastic behavior to the slurry. Since the CB + PVDF G′ and G″ moduli are not affected by the mixing speed, there is the possibility that the changes in the adhesion of NMC + CB and PVDF interaction rule the complete slurry NMC + CB + PVDF. It seems that the NMC + CB + PVDF slurry mixed at 3000 rpm has a much more ideal behavior at the frequencies, from 8 to 25 Hz relative to the coating, because G' ≈ G" [16]. This behavior may result from an adequate CB-absorption balance to NMC without PVDF degradation [16]. In contrast, the slurry mixed at 4000 rpm presents a more

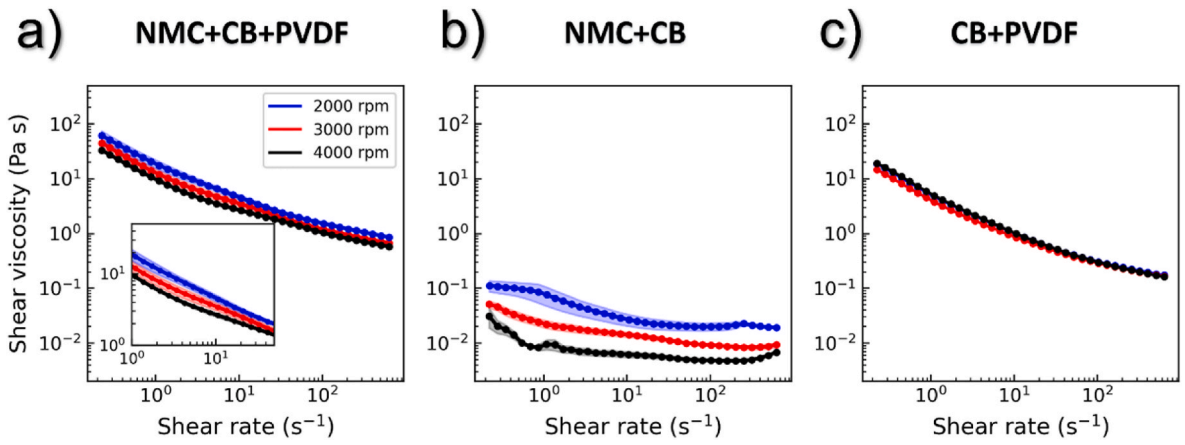

Fig. 1. Rotational viscosity for the slurries for the different slurry compositions presented in Table 1: (a) NMC + CB + PVDF, (b) NMC + CB, and (c) CB + PVDF. The shaded zones correspond to the average deviation after five measurements.

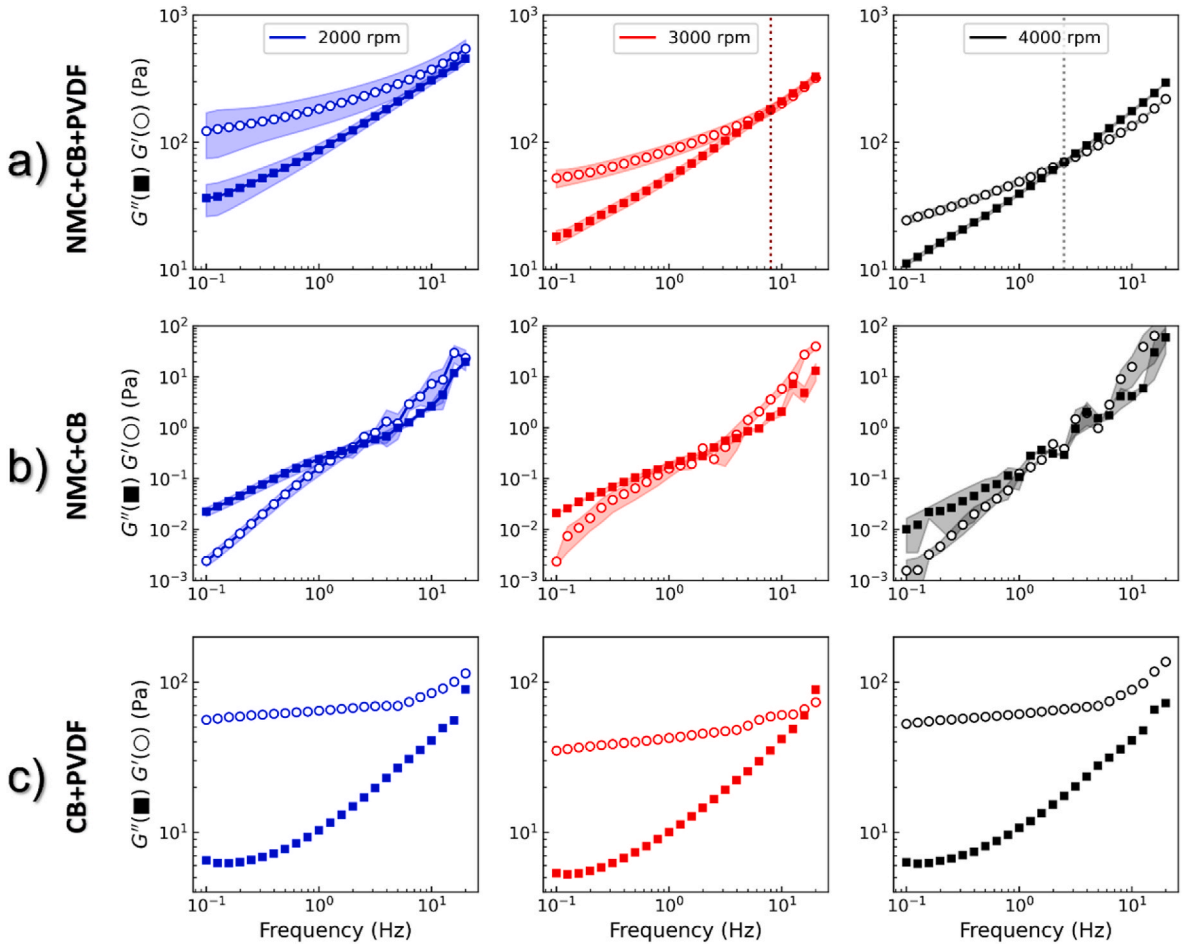

Fig. 2. Oscillatory frequency sweep measurements of slurries at 2000, 3000, and 4000 rpm for the different slurry compositions presented in Table 1: (a) NMC + CB + PVDF, (b) NMC + CB, and (c) CB + PVDF. The shadow zones correspond to the average deviation after five measurements. Markers ■ and ○ refer to G" (viscous modulus) and G' (elastic modulus), respectively.

viscous-like behavior, probably as a result of several reasons, such as carbon black clusters that were broken into fragments, PVDF entangling, formation of shorter polymer chains, and further particle-particle collisions. According to Reynolds et al., an equilibrium of CB adsorption by the NMC in the solution will be the key to avoid instabilities in the slurry and the resulting coating electrodes since having abundant CB in the formulation will cause a gel-like slurry or will lower the energy density of the final coating [16].

3.3. *Mixing speed model: rationalizing the slurry dispersity*

As shown in Fig. 1a and 2a, the viscosity, G', and G" moduli dispersion for the slurry mixed at 2000 rpm are higher than those at 3000 and 4000 rpm. To further understand the origin of the slurry

dispersion, we developed the CGPD model described in the Materials and Methods section and Supporting Information. In our simulation, we focused on studying the effect of mixing speed on the aggregation of AM. It is worth pointing out that we are not simulating the dispersion of solvents or the impact of liquids on the system. Furthermore, because of the treatment of carbon additive and binder as a single entity, our model cannot investigate the effect of mixing speed on the degree of carbon additive aggregation and binder conformation. Nevertheless, in our simulations, we pay more attention to the effect of the mixer on the AM particle-AM particle interaction and the AM particle distribution during the process. In our study, we characterized this phenomenon using the interparticle distance.

In the simulation, we also considered three different mixing speeds. Due to the model's scale being much smaller than the actual electrode slurry mixing dimensions (approximately 1:1000), the simulation did not use rotation speeds that were entirely consistent with the experiments. Here, we refer to simulated mixing speeds as high-speed, medium-speed, and low-speed. The ratio between these three speeds is the same as in the experiment, which is 4:3:2. The same timesteps for mixing and relaxation were used for different mixing speeds in simulations. The simulations were run repeatedly at least two times for each mixing rotation speed, showing excellent reproducibility.

The effect of the slurry mixing speed on the AM-AM particle distance distribution in the slurry was investigated by using the radial distribution function (RDF). Fig. 3a illustrates the RDF of particles within the container. Fig. 3b–d shows the results from the model for the three speeds. The X-axis represents the distance between particle centroids in micrometers, while the Y-axis represents the value of the RDF, denoted as g(r). The RDF indicates the relative density of particles at a specific distance. The height of the peak reflects the increase in particle density at that corresponding distance relative to a uniform distribution, which is the RDF between AM particles at the last timestep of mixing. Low speed shows the first peak at around 8 μm, indicating the presence of smaller relative distances. In comparison, the centrifugal force generated by high-speed rotating mixing increases the distance between particles during mixing. It can be seen that the slurry obtained from low speed also has more peaks, indicating the presence of more structured clusters, which leads to increased polydispersity in the particle organization, resulting in higher variability in the viscosity and G' and G" moduli within the rheology (as shown in Fig. 1a inset and Fig. 2a).

Fig. 4 shows a scheme that illustrates the results obtained by rheology and modeling. We hypothesize that at low speeds, CB may be agglomerated and attached to NMC preferentially. In addition, a high polydispersity of the slurry rheology and more random interparticle distances are obtained, as confirmed by the CGPD model. The obtained viscosity for the lowest mixing speed is higher than at higher speeds, and the slurry presents a viscoelastic liquid-like behavior ($G' > G''$). It could be that this results from the PVDF organization that gives extended polymer chain loops or trains, causing lower polymer adsorption [20]. In contrast, high speeds affect this NMC-CB interaction and distribution of CB in the slurry and the PVDF polymer chains, producing a viscoelastic solid-like behavior ($G'' > G'$). Polymer chains with more loops may probably form, giving a more gel-like behavior [20]. Considering intermediate speeds, the slurry will have an ideal PVDF and CB adsorption to the NMC, giving an in-between viscosity and $G' \approx G''$ in the coating window, with shear rates from 0.6 to $\sim 50\ s^{-1}$.

4. Mixing speed effect on the dried and calendered experimental electrode

Subsequently, we studied the effect of slurry mixing speed on the coated electrode output properties such as porosity, tortuosity factor and microstructure by using a pristine electrode coated using a comma gap of 200 μm, prepared as described in the Methods section. The electrode was also calendered 30 % of the initial thickness to investigate if an intensive calendering degree could amplify differences between the different mixing speeds.

We experimentally studied the effect of the mixing speed on the structural properties by using micro-XCT data and SEM data from the frontal and cross-sectional view. Previously existing Micro-XCT data was used to obtain information on the shape and size of NMC622 particles. Individual AM particles were separated and labeled as single particles by using the commercial software package Avizo. The AM PSDs of the dried electrodes from different mixing speeds were studied, as shown in Fig. 5. It can be observed that the independent PSDs of the three electrodes are essentially consistent, showing that particles with equivalent diameters of about 10–12.5 μm are more abundant. This result is similar to the findings obtained through porosimetry analysis, which indicated an average diameter of 12.6 μm in the powder: 10% of the particles have a diameter of less than 7.17 μm, while 90% of the particles have a diameter of less than 21.0 μm. This indicates that the mixing speed does not significantly impact AM particle fracture in the electrode.

Subsequently, the electrode was calendered from 48% to 24% porosity to exacerbate the differences in the electrode microstructure.

In addition, the tortuosity factor was measured after measuring the impedance of symmetrical cells of the uncalendered and calendered electrode at 24% porosity, as presented in Fig. 6.

While the results show strong similarities for mixing speeds of 2000

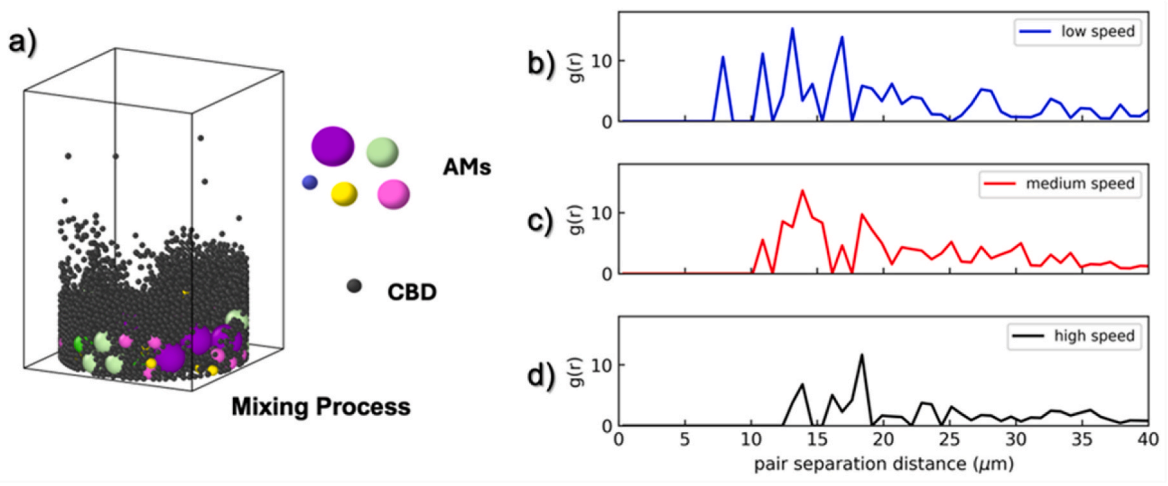

Fig. 3. a) Mixing process simulation representation. The Radial distribution function (RDF) study for the AM-AM particles in the simulation for the different speeds at the last step of the mixing at (b) low speed, (c) medium speed, and (d) high speed.

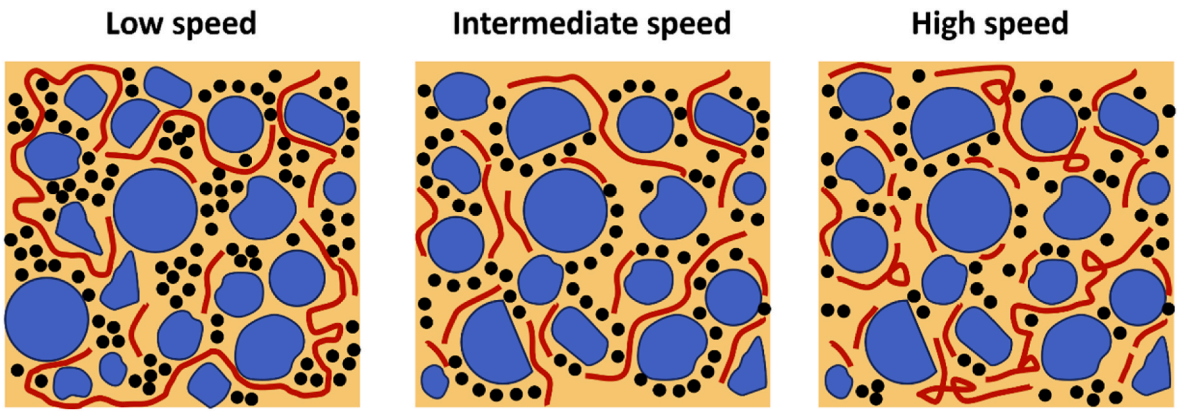

Fig. 4. Scheme of the probable effect of the different speeds in the positive electrode slurry material interaction.

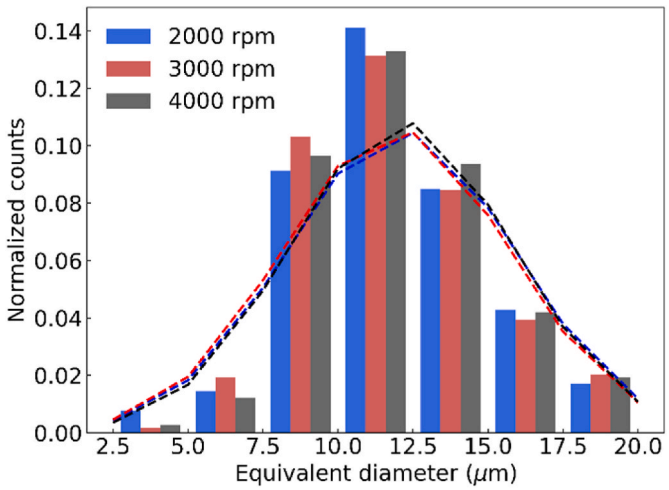

Fig. 5. The PSDs of the dried electrodes from different mixing speeds.

and 3000 rpm, the electrode made from the slurry mixed at 4000 rpm presents a significantly higher tortuosity after calendering. Additionally, 3000 rpm shows a minimum in tortuosity factor for calendered electrodes, although within the experimental error. With the goal of further investigating these effects, stochastically generated structures were analysed to determine tortuosity factors, respecting experimental thicknesses, porosities, and PSDs. The results are presented as follows.

The tortuosity factor and porosity values determined for the coated electrodes, before and after calendering, allow us to study numerically the impact of the mixing speed and the morphology of the CBD on the ionic pathways and, therefore, on electrode performance obtained by stochastic generation from the INNOV algorithm. This allows us to extract conclusions on the casted electrodes.

Electrodes presenting a PSD for the AM similar to the formulation used for preparing the experimental slurry electrode and the CBD were generated stochastically in proportion to their mass ratio, which is 94% AM - 6% CBD. The volume fraction of CBD particles was calculated based on the volume fraction of pores observed experimentally and the CBD mass density, considering 50% nanoporosity before calendering and 27% nanoporosity after calendering. Our INNOV algorithm that can control the morphology of the CBD was used to add it either as films, as aggregates, or as a mix of both. While a direct correlation between mixing speed and CBD morphology is a challenging endeavor, we recreate microstructures with all three configurations to analyse differences, and potentially find insight into the real CBD arrangement at the micrometer scale. As shown in Table 2, each mixing speed corresponds to a porosity observed experimentally and presented in the previous sections. We use these porosities to generate different electrodes for different conditions. Uncalendered and calendered electrodes were studied separately, and two different types of electrodes were generated for each study. Before calendering, one electrode with 47 % porosity (31 % in the bulk and 16 % in the CBD nanopores) called hereafter 47-NC electrode, and one with 48 % porosity (32.3 % in the bulk and 15.7 % in the CBD micropores) called hereafter 48-NC electrode. After calendering, one electrode with 24 % porosity (13.4 % in the

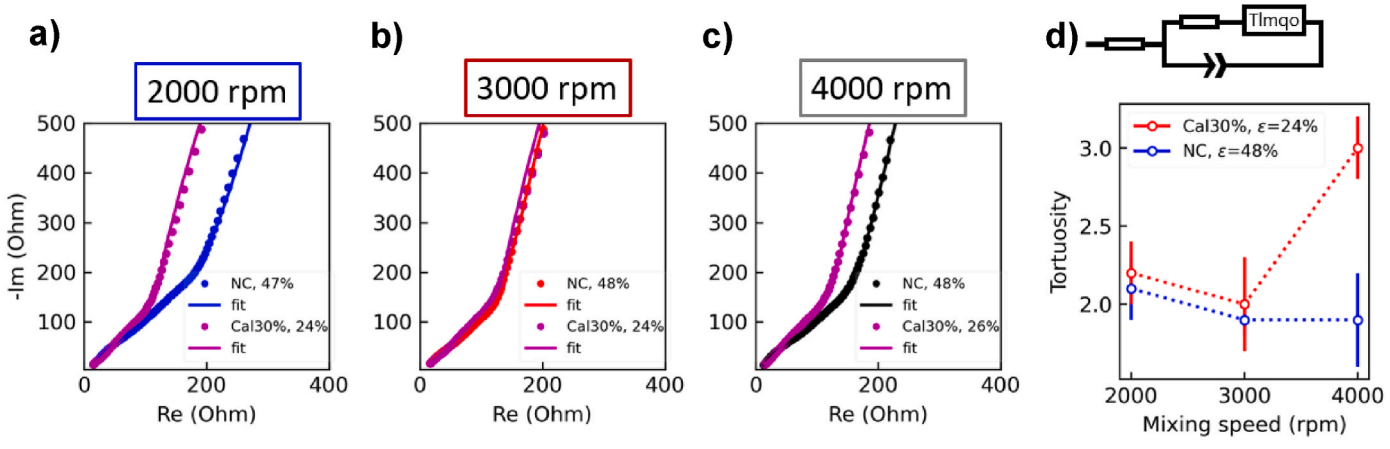

Fig. 6. (a, b, c) EIS spectra of dried and calendred electrode under blocking electrolyte conditions and the corresponding fitting for tortuosity factor determination, d) Tortuosity factor as a function of mixing speed for both dried and calendred electrode.

bulk and 10.6 % in the CBD micropores), called hereafter 24-Cal30% electrode, and one with 26 % porosity (15.7 % in the bulk and 10.3 % in the CBD micropores) called hereafter 26-Cal30% electrode. Each type of electrode was generated three times for a total of six 3D microstructures for each study. For instance, for a calendered electrode, arose two electrodes with CBD as film ($24-Cal30\%_{film}$, $26-Cal30\%_{film}$), two with CBD as aggregate ($24-Cal30\%_{aggregate}$, $26-Cal30\%_{aggregate}$), and two with CBD as mixed ($24-Cal30\%_{mixed}$, $26-Cal30\%_{mixed}$). The 3D microstructures of stochastically generated electrodes are represented in Fig. 7. Each of the conditions (for instance, 26-Cal30% and CBD as film) has been repeated 10 times for the electrode microstructures generations because of their stochastic nature, and results were averaged.

Tortuosity factors for all CBD morphologies depending on the porosity percentages for uncalendered and calendered microstructures are presented respectively in Fig. 8a and b. For each condition, ten calculations are being done and the average across the thickness direction is presented for each CBD morphology. The error bars represent the corresponding spread.

For the uncalendered electrodes, results show statistically insignificant differences when changing CBD morphology (1.7 % dispersion) or when changing porosity values (2.5 % dispersion), as presented in Table 3. However, after calendering, the disparities in tortuosity factor become more pronounced, reaching a 13.5 % decrease in tortuosity factor when porosity increases from 24 % to 26 % and 7.5 % concerning CBD morphology (observed between film and aggregate morphologies for higher porosity).

With these results, a connection can be made to experimental data obtained in the previous sections. After calendering the electrodes obtained at a lower mixing speed, a lower porosity (24%) is obtained with respect to 4000 rpm (26%). The trend in tortuosity factor from stochastic structures here matches the experimental observation. The effect of CBD morphology variation is difficult to elucidate and correlate to experiments due to the narrow dispersion in the results and the fact that stochastic microstructures show opposite effects for 24% and for 26% porosities. We expect that further studies combining experiments and simulations can clarify this, while improving the match between tortuosity factors from experiments and simulations. In the case of uncalendered electrodes, tortuosity factor seems to decrease as mixing speed increases, though the variation is too small to identify a clear trend, both in experiments and simulations.

Two principal conclusions emerge. Firstly, under a compression degree of 30%, a marginal difference in porosity percentage yields a substantial impact on tortuosity factor values. Secondly, the cluster-like morphology for CBD results in an overall higher tortuosity factor under conditions of higher porosity (26 %, obtained for 4000 rpm), while the film-like morphology for CBD results in higher electrode tortuosity factor under conditions of lower porosity (24 %, for 2000 and 3000 rpm).

5. Conclusions

In this work, we have reported a comprehensive systematic study of the influence of the mixing speed in the NMC-based positive electrode slurry rheology through different slurry component combinations. The combinations included mixing the CB and binder (PVDF), the NMC and CB, and the complete slurry composition NMC + CB + PVDF. The rheology of the different mixtures highlights the changes in the nature of the component interactions. For instance, the mixing speed does not affect the CB + PVDF viscosity. In contrast, NMC + CB and NMC + CB + PVDF show higher viscosity changes when the speed increases, highlighting the sensitivity of the NMC + CB network to be broken by shear rate. In addition, frequency oscillatory sweeps were performed on these different mixtures to understand the effect of speed on the slurry behavior. The frequency sweep study on the NMC + CB + PVDF reveals a delicate balance between the G′ and G″ moduli depending on the mixing speed. At lower speeds, the viscoelastic behavior is elastic mainly (G' > G″) with a higher variability. In contrast, the slurry mixed at higher speeds has a viscous-like behavior (G" > G′) and lower variability. In comparison, G′ is almost equal to G″ at intermediate speeds. In contrast, CB + PVDF shows no changes in the elastic behavior (G' > G″) over frequency depending on mixing speed. In addition, NMC + CB presents instabilities in G' and G" when increasing the frequency, highlighting the importance of PVDF in the stability of the slurry network. A model was used to comprehend the viscosity polydispersity, giving hints into the organization of the NMC active material particle distances and their relationship to rheology variation.

Additionally, the casted electrodes data, both before and after calendering was used to stochastically generate virtual electrode microstructures. These allowed us to conclude that very small differences in porosity, on the order of the 1 % that is observed when different mixing speeds are used, result in significant differences in tortuosity factors. With the intention of assigning different CBD morphologies to different mixing speeds, stochastic microstructures can be used and compared to tortuosity measurements, but the variations in both model and experiments make finding this correlation a challenge. We believe that the results presented in this article provide important insights into the mixing protocol, providing guidance towards the optimum manufacturing of battery electrodes.

CRediT authorship contribution statement

Diana Zapata Dominguez: Writing – review & editing, Writing –

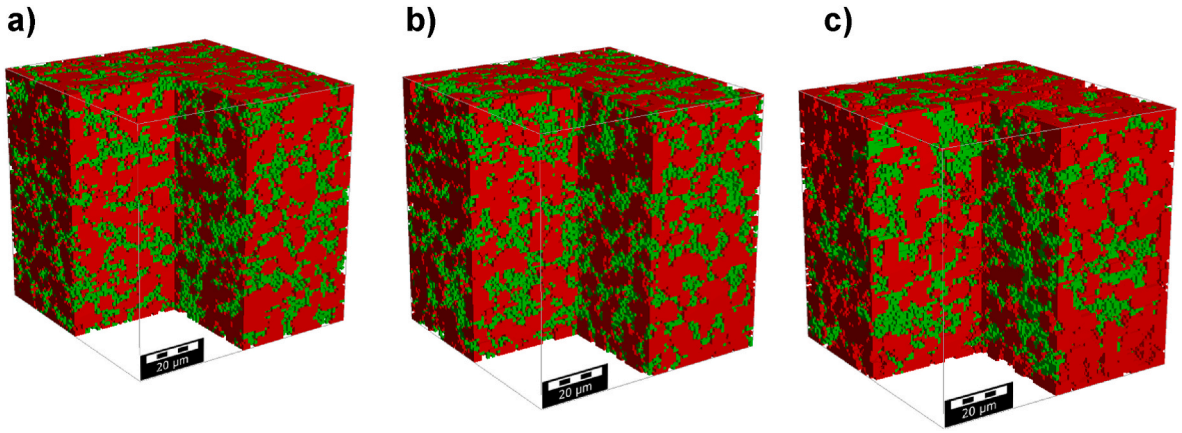

Fig. 7. 3D structures of uncalendred electrode of 47% porosity with NMC in red and CBD in green: (a) $47-NC_{film}$, (b) $47-NC_{mixed}$, (c) $47-NC_{aggregate}$. (For interpretation of the references to color in this figure legend, the reader is referred to the Web version of this article.)

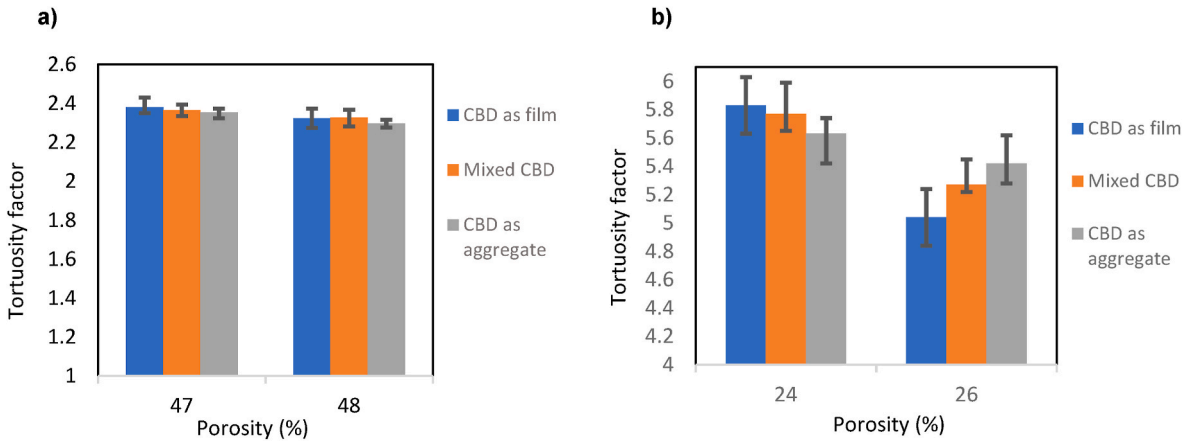

Fig. 8. Tortuosity factor across CBD morphologies. For each morphology, the colored bar represents an average across the thickness coordinate direction: (a) for uncalendered structure, (b) for calendered structure.

Table 3
Tortuosity values in function of CBD morphology and in function of porosity percentages.

CBD Morphology	Film				Mixed				Aggregate			
Porosity [%]	47	48	24	26	47	48	24	26	47	48	24	26
Tortuosity factor	2.38	2.32	5.83	5.04	2.36	2.33	5.77	5.27	2.35	2.29	5.63	5.42

original draft, Visualization, Methodology, Investigation, Formal analysis, Data curation, Conceptualization. **Jiahui Xu:** Writing – review & editing, Writing – original draft, Investigation, Formal analysis, Data curation. **Yasmina Boudjema:** Writing – review & editing, Writing – original draft, Formal analysis, Data curation. **Siwar Ben Hadj Ali:** Writing – review & editing, Writing – original draft, Formal analysis, Data curation. **Franco M. Zanotto:** Writing – review & editing, Writing – original draft, Formal analysis, Data curation. **Alejandro A. Franco:** Writing – review & editing, Writing – original draft, Supervision, Resources, Project administration, Funding acquisition, Formal analysis, Data curation, Conceptualization.

Declaration of competing interest

The authors declare that they have no known competing financial interests or personal relationships that could have appeared to influence the work reported in this paper.

Data availability

Data will be made available on request.

Acknowledgments

A.A.F., D.Z.D., and J.X. acknowledge the European Union's Horizon 2020 research and innovation program for funding support through the European Research Council (grant agreement 772873, ARTISTIC project). S.B.H.A. and A.A.F. acknowledge the support by Umicore within the DESTINY PhD Programme, which has received funding from European Union's Horizon 2020 research and innovation programme under the Marie Skłodowska-Curie Actions COFUND (Grant Agreement 945357). A.A.F., D.Z.D., and J.X. acknowledge Dr. Arnaud Demortière (LRCS) for the guidance in the electrode tomography characterizations. A.A.F. and F.M.Z. acknowledge the European Union's Horizon Europe research and innovation programme under grant agreement No. 101069686 (PULSELiON project). A.A.F. acknowledges the Institut Universitaire de France for its support.

Appendix B. Supplementary data

Supplementary data to this article can be found online at https://doi.org/10.1016/j.powera.2024.100141.

Appendix A. Supplementary data

Supplementary data to this article can be found online.

References

[1] J. Li, J. Fleetwood, W.B. Hawley, W. Kays, From materials to cell: state-of-the-art and prospective technologies for lithium-ion battery electrode processing, Chem. Rev. 122 (2022) 903–956, https://doi.org/10.1021/acs.chemrev.1c00565.
[2] F.M. Zanotto, D.Z. Dominguez, E. Ayerbe, I. Boyano, C. Burmeister, M. Duquesnoy, M. Eisentraeger, J.F. Montaño, A. Gallo-Bueno, L. Gold, F. Hall, N. Kaden, B. Muerkens, L. Otaegui, Y. Reynier, S. Stier, M. Thomitzek, A. Turetskyy, N. Vallin, J. Wessel, X. Xu, J. Abbasov, A.A. Franco, Data specifications for battery manufacturing digitalization: current status, challenges, and opportunities, Batter. Supercaps. 5 (2022), https://doi.org/10.1002/batt.202200224.
[3] R. Schmuch, R. Wagner, G. Hörpel, T. Placke, M. Winter, Performance and cost of materials for lithium-based rechargeable automotive batteries, Nat. Energy 3 (2018) 267–278, https://doi.org/10.1038/s41560-018-0107-2.
[4] D. Grießl, A. Adam, K. Huber, A. Kwade, Effect of the slurry mixing process on the structural properties of the anode and the resulting fast-charging performance of the lithium-ion battery cell, J. Electrochem. Soc. 169 (2022) 020531, https://doi.org/10.1149/1945-7111/ac4cdb.
[5] M. Wang, D. Dang, A. Meyer, R. Arsenault, Y.-T. Cheng, Effects of the mixing sequence on making lithium ion battery electrodes, J. Electrochem. Soc. 167 (2020) 100518, https://doi.org/10.1149/1945-7111/ab95c6.
[6] W.B. Hawley, J. Li, Beneficial rheological properties of lithium-ion battery cathode slurries from elevated mixing and coating temperatures, J. Energy Storage 26 (2019) 100994, https://doi.org/10.1016/j.est.2019.100994.
[7] J.K. Mayer, L. Almar, E. Asylbekov, W. Haselrieder, A. Kwade, A. Weber, H. Nirschl, Influence of the carbon black dispersing process on the microstructure and performance of Li-ion battery cathodes, Energy Technol. 8 (2020), https://doi.org/10.1002/ente.201900161.
[8] E. Asylbekov, R. Trunk, M.J. Krause, H. Nirschl, Microscale discrete element method simulation of the carbon black aggregate fracture behavior in a simple shear flow, Energy Technol. 9 (2021), https://doi.org/10.1002/ente.202000850.
[9] E. Asylbekov, J. Mayer, H. Nirschl, A. Kwade, Modeling of carbon black fragmentation during high-intensity dry mixing using the population balance equation and the discrete element method, Energy Technol. 11 (2023), https://doi.org/10.1002/ente.202200867.
[10] T. Lombardo, J. Hoock, E.N. Primo, A.C. Ngandjong, M. Duquesnoy, A.A. Franco, Accelerated optimization methods for force-field parametrization in battery

electrode manufacturing modeling, Batter. Supercaps. 3 (2020) 721–730, https://doi.org/10.1002/batt.202000049.
[11] M. Duquesnoy, T. Lombardo, F. Caro, F. Haudiquez, A.C. Ngandjong, J. Xu, H. Oularbi, A.A. Franco, Functional data-driven framework for fast forecasting of electrode slurry rheology simulated by molecular dynamics, npj Comput. Mater. 8 (2022) 161, https://doi.org/10.1038/s41524-022-00819-2.
[12] A.P. Thompson, H.M. Aktulga, R. Berger, D.S. Bolintineanu, W.M. Brown, P. S. Crozier, P.J. in 't Veld, A. Kohlmeyer, S.G. Moore, T.D. Nguyen, R. Shan, M. J. Stevens, J. Tranchida, C. Trott, S.J. Plimpton, Lammps - a flexible simulation tool for particle-based materials modeling at the atomic, meso, and continuum scales, Comput. Phys. Commun. 271 (2022) 108171, https://doi.org/10.1016/j.cpc.2021.108171.
[13] Mehdi Chouchane, A. Alejandro, Franco, cover feature: an invitation to engage with computational modeling: user-friendly tool for in silico battery component generation and meshing, Batteries & Supercaps (2021), https://doi.org/10.1002/batt.202100202.
[14] Teo Lombardo, et al., Experimentally validated three-dimensional modeling of organic-based sodium-ion battery electrode manufacturing, Batteries & Supercaps (2022), https://doi.org/10.1002/batt.202200116.
[15] C.D. Reynolds, P.R. Slater, S.D. Hare, M.J.H. Simmons, E. Kendrick, A review of metrology in lithium-ion electrode coating processes, Mater. Des. 209 (2021) 109971, https://doi.org/10.1016/j.matdes.2021.109971.
[16] C.D. Reynolds, S.D. Hare, P.R. Slater, M.J.H. Simmons, E. Kendrick, Rheology and structure of lithium-ion battery electrode slurries, Energy Technol. 10 (2022) 2200545, https://doi.org/10.1002/ente.202200545.
[17] K. Kuratani, K. Ishibashi, Y. Komoda, R. Hidema, H. Suzuki, H. Kobayashi, Controlling of dispersion state of particles in slurry and electrochemical properties of electrodes, J. Electrochem. Soc. 166 (2019) A501–A506, https://doi.org/10.1149/2.0111904jes.
[18] Y. Komoda, K. Ishibashi, K. Kuratani, R. Hidema, H. Suzuki, H. Kobayashi, Rheological interpretation of the structural change of LiB cathode slurry during the preparation process, JCIS Open 5 (2022) 100038, https://doi.org/10.1016/j.jciso.2021.100038.
[19] M. Yoo, C.W. Frank, S. Mori, Interaction of poly(vinylidene fluoride) with graphite particles. 1. Surface morphology of a composite film and its relation to processing parameters, Chem. Mater. 15 (2003) 850–861, https://doi.org/10.1021/cm0209970.
[20] W. Bauer, D. Nötzel, Rheological properties and stability of NMP based cathode slurries for lithium ion batteries, Ceram. Int. 40 (2014) 4591–4598, https://doi.org/10.1016/j.ceramint.2013.08.137.